Intelligent Control of Microgrid With Virtual Inertia Using Recurrent Probabilistic Wavelet Fuzzy Neural Network

Kuang-Hsiung Tan, Faa-Jeng Lin, *Fellow, IEEE*, Cheng-Ming Shih, and Che-Nan Kuo

***Abstract*—A microgrid with virtual inertia using master–slave control is proposed in this article to overcome the drawbacks of traditional inverter-based distributed generators for lack of inertia and without grid-forming capability. The microgrid using master–slave control is composed of a storage system, a photovoltaic (PV) system and a varying resistive three-phase load. The storage system and PV system are regarded as the master unit and the slave unit, respectively, in the microgrid. Moreover, in order to improve the reactive power control in grid-connected mode and the transient response of microgrid during the switching between the grid-connected mode and islanding mode, an online trained recurrent probabilistic wavelet fuzzy neural network (RPWFNN) is proposed to replace the conventional proportional-integral (PI) controller in the storage system. Furthermore, when the microgrid is operated in islanding mode, the load variation will have serious influence on the voltage control of the microgrid. Thus, the RPWFNN control is also proposed to improve the transient and steady-state responses of voltage control in the microgrid. Finally, according to some experimental results, excellent control performance of the microgrid with virtual inertia using the proposed intelligent controller can be achieved.**

***Index Terms*—Fuzzy neural network, grid-forming, microgrid, virtual inertia.**

I. Introduction

NOWADAYS, due to the growing awareness of energy crisis and environmental concerns, the penetration of distributed generations (DGs) using renewable energy source has been significantly increased in the power system [1], [2]. Thus, a novel concept of microgrid, which integrates the loads and the DGs at customer side and can be operated in either grid-connected mode or islanding mode, has been arisen in the power system. The microgrid is regarded as a small-scale power system and can improve grid performance and provide flexibility to its operation [2], [4]. Hence, many different microgrids have been developed and deployed in different areas and countries [5], [6]. Moreover, in the past decade, several control strategies and energy management for the microgrid had been investigated [7]–[10]. The control algorithms of the DGs in microgrid can be generally divided into two categories: master–slave control and droop control [7]. The main purpose of the master–slave control is to ensure the outputs of the DGs of the microgrid to track the active/reactive power commands or voltage/frequency commands [9], [10]. In other words, one of the DGs is regarded as the master unit and operated under the active/reactive power control in grid-connected mode. When the microgrid is operated in islanding mode, the master unit is switched from the active/reactive power control to the voltage/frequency control to maintain the voltage and frequency of the microgrid. The rest of the DGs are regarded as the slave units and operated under the active/reactive power control in both grid-connected mode and islanding mode [2]. The merits of the master–slave control are the relatively low risk and easy to be implemented technically [8], [10]. On the other hand, the droop control is based on the active power/frequency and reactive power/voltage droop characteristics of the DGs to supply the suitable commands for DGs. Furthermore, the main advantages of the droop control are that it does not need communications between the DGs of the microgrid and just using the local measurements can achieve the "plug and play" function of the DGs [8], [11], [12]. However, due to the presence of the uncertainties of the output impedance and the neglect of the load dynamics, the droop control cannot provide the accurate power sharing among the DGs [8]. In addition, if the loads are nonlinear, the droop control is unsuitable to be adopted owing to its disregarding of harmonic currents [8].

Conventional grid-connected power converters are normally operated as current sources and have no any frequency regulation capability. Therefore, the power system will be unstable resulted from the lack of rotating inertia if a large amount of inverter-based DGs is deployed [12]–[14]. In other words, the dynamic responses of the inverter-based DGs are much faster than the conventional synchronous generator (SG) that will make the power system susceptible to oscillation resulting from sudden load variations or external disturbances [12], [15]. On the other hand, the SG possesses the ability of injecting the kinetic energy preserved in the rotating inertia to the power grid or absorbing the extra power energy in the rotating inertia when sudden load

---

Manuscript received June 17, 2019; revised September 10, 2019; accepted November 15, 2019. Date of publication November 18, 2019; date of current version March 13, 2020. This work was supported by the Ministry of Science and Technology of Taiwan, R.O.C. under Grant MOST 108-3116-F-008-001. Recommended for publication by Associate Editor J. M. Guerrero. *(Corresponding author: Kuang-Hsiung Tan.)*

K.-H. Tan is with the Department of Electrical and Electronic Engineering, Chung Cheng Institute of Technology, National Defense University, Taoyuan 335, Taiwan (e-mail: s913115@gmail.com).

F.-J. Lin, C.-M. Shih, and C.-N. Kuo are with the Department of Electrical Engineering, National Central University, Chungli 320, Taiwan (e-mail: linfj@ee.ncu.edu.tw; stoneshih914@gmail.com; phes02201@gmail.com).

Color versions of one or more of the figures in this article are available online at http://ieeexplore.ieee.org.

Digital Object Identifier 10.1109/TPEL.2019.2954740

variations or external disturbances occur. Owing to the merit of the robustness of the rotating inertia, a lot of literature for the inverter-based DGs using a virtual synchronous generator (VSG) have been developed to emulate the virtual inertia by using the essential swing equation to mimic the transient characteristics of SG [11], [16]–[19]. In [17], a full converter wind turbine with short-term minute-level energy storage adopted VSG control to represent the dynamic behavior of SG for supporting the power grid. Moreover, an improved VSG with bounded voltage and frequency has been proposed in [18] for smart grid integration. Furthermore, a new robust control adopted virtual inertia control to improve the frequency stability of an islanding microgrid was proposed in [19]. However, the adoption of VSG for the control strategies of microgrid are almost based on the droop control [11], [20]. There was seldom literature to develop the master–slave control using virtual inertia for the operation of microgrid.

Since fuzzy neural network (FNN) control comprises the merits of both fuzzy logic control and neural network control, there are many research works using different FNN control algorithms in industrial applications [21], [22]. In [21], a grid-connected three-phase squirrel-cage induction generator system using wavelet fuzzy neural network (WFNN) control is proposed to improve the tracking control of the dc-link voltage for wind power applications. Moreover, an active islanding detection method using WFNN control for the detection of islanding phenomenon was proposed in [22]. The WFNN owns the following advantages:

1) the capability to approximate the nonlinear systems and uncertainties [21], [22];
2) the ability of WNN in pattern classification or forecast problems [23];
3) the wavelet decomposition property [24];
4) the abilities of FNN in learning, generalization, parallel computation, and handling uncertain information.

Furthermore, the probabilistic neural network (PNN) was a feedforward neural network proposed by Specht [25]. The PNN owns the probability density function estimator and the Bayes classification rule [26]. Hence, the PNN possesses the superior modeling performance and adaptability to cope with the system uncertainties effectively. In addition, the PNN has been extensively utilized in the different issues such as image classification, fault detection, earthquake magnitude prediction, nonlinear mapping, and phoneme recognition [25]–[27]. Additionally, the recurrent neural network (RNN) is developed to model the dependency in sequences by using cyclic connections of the neurons [27]–[29]. In other words, the RNN adopts the internal feedback loops of recurrent neurons to incorporate the temporal dependence and context information [28]. Therefore, the RNN has the capability to achieve the dynamic modeling behavior and the ability to cope with the time-varying inputs or outputs [27]. The RNN has been comprehensively adopted in optimization problems, signal processing, and pattern recognition [27], [30], [31]. In [30], a network traffic classifier using RNN to improve the performance of the monitoring systems. A waveform modeling and generation method using RNN for speech bandwidth extension was proposed in [31]. An online trained recurrent probabilistic wavelet fuzzy neural network (RPWFNN), which comprises the merits of the WFNN, PNN, and RNN, is proposed in this article to improve the control performance of the microgrid.

There are three main concerns in the operation of the microgird.

1) Low-voltage ride through (LVRT) in grid-connected mode.
2) Smoothly switching between grid-connected mode and islanding mode.
3) Grid-forming capability in islanding mode.

When the microgrid is operated in grid-connected mode, the grid codes demand the DGs have the LVRT ability to help to sustain the stability of the power system, especially during the grid faults. Hence, the reactive power control should be immediately responded during the grid faults according to the grid codes [32]. Moreover, the transient responses of three-phase voltages and currents in the microgrid during the switching between the grid-connected mode and islanding mode will cause serious influence on the customers' loads. Furthermore, in islanding mode, the load variation will affect the stability of the microgrid. Therefore, in this article, a microgrid with virtual inertia using the master–slave control algorithm is developed to overcome the drawbacks of inverter-based DGs for lack of the rotating inertia and without grid-forming capability. The developed microgrid comprises a storage system, a photovoltaic (PV) system, and a varying resistive three-phase load. The storage system and PV system are designed as the master unit and the slave unit, respectively. In addition, the intelligent RPWFNN controller is proposed to replace the conventional proportional-integral (PI) controller in the storage system to improve the reactive power control performance in grid-connected mode and the transient response during the mode switching. Additionally, the online trained RPWFNN control is also proposed in the storage system to improve the transient and steady-state responses of voltage control in islanding mode under load variation. In this article, the operating theories of the microgird with virtual inertia using a master–slave control algorithm will be detailedly depicted in Section II. The network structure and online learning algorithms of the proposed RPWFNN controller will be expressed in Section III. Then, in Section IV, the effectiveness and feasibility of the microgrid with virtual inertia using the proposed RPWFNN controller to improve the reactive power control performance in grid-connected mode, the smoothly switching response between the grid-connected mode and islanding mode, and the voltage control response in islanding mode under load variation will be demonstrated by some experimental results. Finally, Section V concludes this article.

II. Microgrid With Virtual Inertia Using Master–Slave Control

In this article, the architecture of the developed microgrid is illustrated in Fig. 1. The microgrid comprises the storage system, PV system, and a varying resistive three-phase load. The storage system and PV system are designed to be the master and the slave units, respectively. The load is connected with the

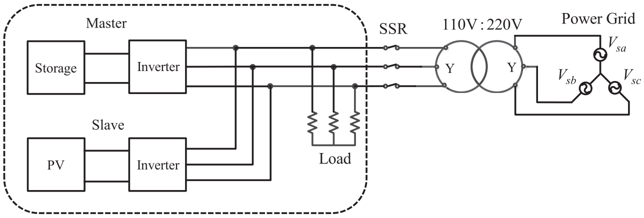

Fig. 1. Architecture of developed microgrid.

storage and PV systems in parallel to form the microgrid. The three-phase voltage of the microgrid is 110 V rms. Moreover, the microgrid is connected with the three-phase power grid through a static switch relay (SSR) and a Y-Y connected transformer for transferring the voltage to a 220 V rms distributed network.

A. Master Control With Virtual Inertia

The control block of the microgrid using master–slave control is provided in Fig. 2. The storage system using active/reactive power control in grid-connected mode is shown in Fig. 2(a). In this mode, the frequency and voltage of the microgrid are imposed by the power grid. In Fig. 2(a), first, the three-phase voltages $V_a,\ V_b,\ V_c$ of the microgrid and the three-phase current $i_{oa},\ i_{ob},\ i_{oc}$ of the storage system are measured for the power calculation and synchronizing with the power grid through the phase-lock-loop (PLL). The three-phase voltages $V_a,\ V_b,\ V_c$ and the three-phase currents $i_{oa},\ i_{ob},\ i_{oc}$ are transferred to *dq* synchronous reference frame as follows:

$$\begin{bmatrix} V_d \\ V_q \\ V_0 \end{bmatrix} = \frac{2}{3} \begin{bmatrix} \cos\theta_e & \cos\left(\theta_e - \frac{2}{3}\pi\right) & \cos\left(\theta_e + \frac{2}{3}\pi\right) \\ \sin\theta_e & \sin\left(\theta_e - \frac{2}{3}\pi\right) & \sin\left(\theta_e + \frac{2}{3}\pi\right) \\ \frac{1}{2} & \frac{1}{2} & \frac{1}{2} \end{bmatrix} \begin{bmatrix} V_a \\ V_b \\ V_c \end{bmatrix} \tag{1}$$

$$\begin{bmatrix} i_d \\ i_q \\ i_0 \end{bmatrix} = \frac{2}{3} \begin{bmatrix} \cos\theta_e & \cos\left(\theta_e - \frac{2}{3}\pi\right) & \cos\left(\theta_e + \frac{2}{3}\pi\right) \\ \sin\theta_e & \sin\left(\theta_e - \frac{2}{3}\pi\right) & \sin\left(\theta_e + \frac{2}{3}\pi\right) \\ \frac{1}{2} & \frac{1}{2} & \frac{1}{2} \end{bmatrix} \begin{bmatrix} i_{oa} \\ i_{ob} \\ i_{oc} \end{bmatrix} \tag{2}$$

where $V_d,\ V_q,$ and V_0 are the *dq0*-axis voltages of the microgrid; $i_d,\ i_q,$ and i_0 are the *dq0*-axis currents of the storage system; and θ_e is the synchronous angle obtained by the PLL. Hence, the active power output P_m and reactive power output Q_m of the storage system are calculated in the following:

$$P_m = \frac{3}{2}(V_q i_q + V_d i_d) \tag{3}$$

$$Q_m = \frac{3}{2}(V_q i_d - V_d i_q). \tag{4}$$

According to the PLL algorithm, the *d*-axis voltage V_d shown in (3) and (4) are set to be zero for the synchronization with the power grid. Hence, the active power P_m and reactive power Q_m are proportional to i_q and i_d currents respectively in the following:

$$P_m = \frac{3}{2} V_q i_q \tag{5}$$

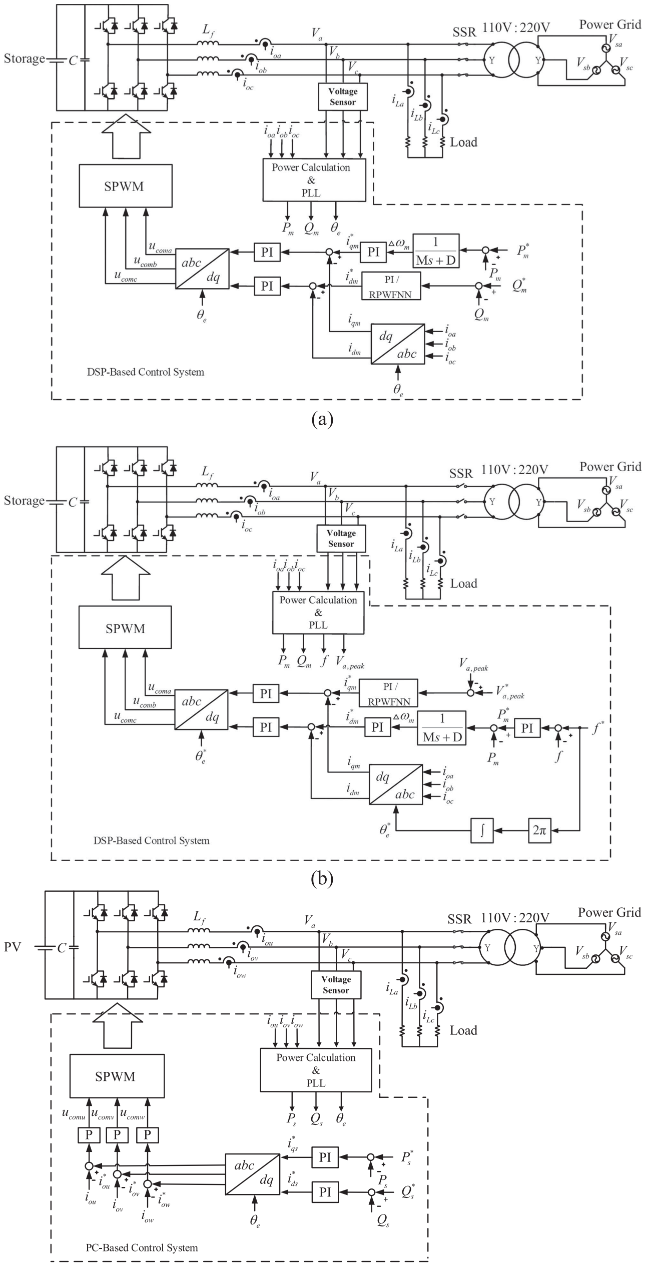

(a)

(b)

(c)

Fig. 2. Control blocks of master–slave algorithm in microgrid. (a) Active and reactive power control of storage system with virtual inertia in grid-connected mode. (b) Voltage and frequency control of storage system with virtual inertia in islanding mode. (c) Active and reactive power control of PV system in both grid-connected and islanding modes.

$$Q_m = \frac{3}{2} V_q i_d. \tag{6}$$

Furthermore, in this article, in order to emulate the rotating inertia in the microgrid, the swing equation of SG is added in the storage system as follows [13], [33], [34]:

$$M \frac{d \bigtriangleup \omega_m}{dt} = P^*_m - P_m - D \bigtriangleup \omega_m \tag{7}$$

where M is the inertia constant; $\bigtriangleup \omega_m$ is the virtual angular velocity deviation in SG; *D* is the damping factor; P^*_m is the active power command of the storage system. By using the Laplace transform, the swing equation of SG can be redescribed as

$$\triangle\,\omega_m = \frac{P_m^* - P_m}{Ms + D}. \tag{8}$$

Then, the q-axis control current i_{qm}^* for the active power control is generated by a PI controller. Meanwhile, the d-axis control current i_{dm}^* for the reactive power control is obtained through a PI or the proposed RPWFNN controller using the reactive power error as input. Finally, the control signals $u_{\text{coma}},\ u_{\text{comb}},\ u_{\text{comc}}$ are computed through the dq/abc coordinate transformation to obtain the sinusoidal pulsewidth modulation (SPWM) switching signals for the storage system operated in grid-connected mode.

When the power grid is failed, the microgrid can immediately disconnect from the power grid via the SSR and smoothly switch the control mode from the active/reactive power control to the voltage/frequency control as shown in Fig. 2(b) to control the voltage and frequency of the microgrid. In Fig. 2(b), the peak value of the a-phase voltage $V_{a,\text{peak}}$ and the frequency f of the microgrid are obtained by using the frequency detector. Then, the peak value of the a-phase voltage $V_{a,\text{peak}}$ and the frequency f of the microgrid are compared with the peak value of the phase voltage command $V_{a,\text{peak}}^*$ and the frequency command f^*. Thus, the q-axis control current i_{qm}^* for the voltage control is obtained through a PI or the proposed RPWFNN controller. Meanwhile, the d-axis control current i_{dm}^* is obtained through the swing equation shown in (8) and a PI controller for maintaining the frequency of the microgrid. Finally, the control signals $u_{\text{coma}},\ u_{\text{comb}},\ u_{\text{comc}}$ are calculated through the dq/abc coordinate transformation with the angle command θ_e^* to obtain the SPWM switching signals for the storage system operated in islanding mode.

B. *Slave Control*

In this article, the PV system is regarded as the slave unit and can provide active power and reactive power control in both the grid-connected mode and islanding mode. The control block of the PV system is illustrated in Fig. 2(c). The three-phase voltages $V_a,\ V_b,\ V_c$ of the microgrid and the three-phase currents $i_{ou},\ i_{ov},\ i_{ow}$ of the PV system are detected and transferred to *dq* synchronous reference frame for the power calculation and synchronization. The errors of the active power and reactive power are both sent to the PI controllers for the generations of the *dq*-axis control currents i_{qs}^* and i_{ds}^*, respectively. Moreover, the three-phase current commands $i_{ou}^*,\ i_{ov}^*,\ i_{ow}^*$ are calculated through the dq/abc coordinate transformation. Finally, the control signals $u_{\text{comu}},\ u_{\text{comv}},\ u_{\text{comw}}$ are computed to obtain the SPWM switching signals for the PV system.

III. NETWORK STRUCTURE AND ONLINE LEARNING ALGORITHM FOR RPWFNN

In this article, to improve the reactive power control of the storage system operated in grid-connected mode, the transient response during the mode switching, and the voltage control in islanding mode under load variation, an online trained RPWFNN controller is first proposed to replace the conventional PI controller in the storage system of the microgrid. The network structure and the online learning based on the backpropagation (BP) algorithm of the proposed RPWFNN are depicted in detail as follows.

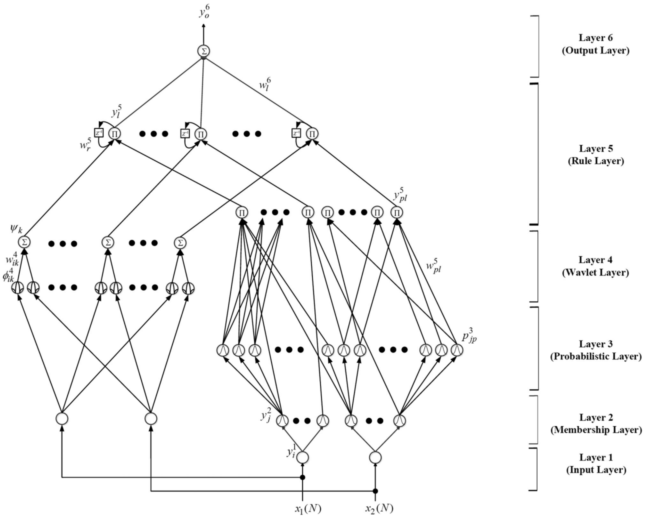

Fig. 3. Network structure of proposed RPWFNN.

A. *Network Structure*

The network structure of the proposed RPWFNN with two inputs and one output is presented in Fig. 3. The proposed RPWFNN comprises the input layer, the membership layer, the probabilistic layer, the wavelet layer, the rule layer, and the output layer. The detailed signal propagation and the relationship of each layer are expressed as follows.

1) Layer 1 (Input Layer): The relationship between the input and output of this layer are represented in the following:

$$\text{net}_i^1(N) = x_i^1 \tag{9}$$

$$y_i^1(N) = f_i^1(\text{net}_i^1(N)) = \text{net}_i^1(N), \quad i = 1,\ 2 \tag{10}$$

where x_i^1 expresses the *i*th input to the input layer; *N* depicts the *N*th iteration. In this article, the inputs of the proposed RPWFNN are the reactive power error $x_1^1(N) = e = Q_m^* - Q_m$ of the storage system operated in grid-connected mode or the *a*-phase voltage error $x_1^1(N) = e = V_{a,\text{peak}}^* - V_{a,\text{peak}}$ of the storage system operated in islanding mode and its derivative $x_2^1(N) = \dot{e}$.

2) Layer 2 (Membership Layer): In this layer, the Gaussian functions are adopted to implement the fuzzification operation in the proposed RPWFNN. The input and output of the node in this layer are expressed as follows:

$$\text{net}_j^2(N) = -\frac{\left(y_i^1 - m_{ij}^2\right)^2}{\left(\sigma_{ij}^2\right)^2} \tag{11}$$

$$y_j^2(N) = f_j^2(\text{net}_j^2(N)) = \exp(\text{net}_j^2(N)), \quad j = 1,\ 2, \ldots,\ 6 \tag{12}$$

where $y_j^2(N)$ are the node output of membership layer; and m_{ij}^2 and σ_{ij}^2, respectively, are the mean and standard deviation of the Gaussian function in the *j*th term associated with the *i*th input variable.

3) Layer 3 (Probabilistic Layer): The Gaussian functions are also chosen as the receptive field function in this layer and represented as follows:

$$\mathrm{net}_{jp}^3(N) = -\frac{\left(y_j^2(N) - m_{jp}^3\right)^2}{\left(\sigma_{jp}^3\right)^2} \tag{13}$$

$$p_{jp}^3(N) = f_{jp}^3(\mathrm{net}_{jp}^3(N)) = \exp(\mathrm{net}_{jp}^3(N)), \quad p = 1,\ 2,\ 3 \tag{14}$$

where $p_{jp}^3(N)$ are the node output of the probabilistic layer; m_{jp}^3 and σ_{jp}^3 are the mean and standard deviation of the Gaussian function in the *p*th term associated with the *j*th input variable.

4) Layer 4 (Wavelet Layer): The wavelet layer includes k wavelet functions (WFs). The WFs are depicted in the following and ψ_k is the consequence of the WFs

$$\phi_{ik}^4(N) = \frac{1}{\sqrt{|\sigma_{ik}^4|}}\left[1 - \frac{\left(x_i^1(N) - m_{ik}^4\right)^2}{\left(\sigma_{ik}^4\right)^2}\right] \times \exp\left[-\frac{\left(x_i^1(N) - m_{ik}^4\right)^2}{2\left(\sigma_{ik}^4\right)^2}\right] i = 1,2; k = 1,2,\ldots,9 \tag{15}$$

$$\psi_k(N) = \sum w_{ik}^4 \phi_{ik}^4(N) \tag{16}$$

where ψ_k is *k*th term WFs output to the node of the wavelet layer; w_{ik}^4 is the wavelet weight in the WFs layer; and ϕ_{ik}^4 is *i*th in the *k*th term wavelet output to the node of wavelet sum layer.

5) Layer 5 (Rule Layer): In the rule layer, each node is denoted by $\prod$, which performs the product operation to obtain the Mamdani inference set. The probabilistic information is processed using Bayes' theorem in consideration of the group of the fuzzy grade being independent variables, as shown in (17). Moreover, in order to achieve the recurrent property, the output of each rule node is fed back to itself as inputs. Hence, the previous values can be memorized by feedback structure, as shown in (18). Furthermore, the wavelet outputs are also proceeded in (18). The node outputs of this layer are expressed in the following:

$$y_{pl}^5(N) = \prod_{j,p} w_{pl}^5 y_j^2 p_{jp}^3, \quad j = 1,2,\ldots,6; \quad p = 1,2,3 \tag{17}$$

$$\mathrm{net}_l^5(N) = y_{pl}^5 \psi_k w_r^5 y_l^5(N-1) \tag{18}$$

$$y_l^5(N) = f_l^5(\mathrm{net}_l^5(N)), \quad l = 1,2,\ldots,9 \tag{19}$$

where w_{pl}^5 is the connective weight between the rule layer and the probabilistic layer, which is set to be 1; w_r^5 is the connective weight of the node and is also the recurrent property; and y_l^5 is the output of the rule layer.

6) Layer 6 (Output Layer): In this layer, the input and output of node are depicted in the following:

$$\mathrm{net}_o^6(N) = \sum_{l=1}^{9} w_l^6 y_l^5(N), \quad o = 1 \tag{20}$$

$$y_o^6(N) = f_o^6(\mathrm{net}_o^6(N)) \tag{21}$$

where $y_o^6(N)$ is the output of the proposed RPWFNN, which is the current i_{dm}^* of storage system operated in the grid-connected mode for the reactive power control and the current i_{qm}^* of storage system operated in islanding mode for the voltage control, respectively; and w_l^6 is the connective weight between the rule layer and the output layer.

B. Online Learning Algorithm

In accordance with the supervised gradient decent method, the proposed RPWFNN possesses the online learning ability. The online learning of the proposed RPWFNN can be achieved by using the chain rule for the derivation of an error function in respect to the variables of the network. In this article, the reactive power control of the storage system operated in grid-connected mode is derived for example. In the beginning, an energy function $E(N)$ is defined as follows:

$$E(N) = \frac{1}{2}(Q_m^* - Q_m)^2 = \frac{1}{2}e^2. \tag{22}$$

The main objective is to minimize the error function $E(N)$ to gain the online learning parameters. The online learning algorithm is detailedly depicted as follows.

1) Layer 6: The propagated error term is expressed as

$$\delta_o^6 = -\frac{\partial E}{\partial y_o^6(N)} = -\frac{\partial E}{\partial Q_m}\frac{\partial Q_m}{\partial y_o^6(N)}. \tag{23}$$

The updated amount of the connective weight in this layer is described as

$$\Delta w_l^6 = -\eta_1 \frac{\partial E}{\partial w_l^6} = -\eta_1 \frac{\partial E}{\partial y_o^6(N)}\frac{\partial y_o^6(N)}{\partial w_l^6} = \eta_1 \delta_o^6 x_l^6 \tag{24}$$

where η_1 is the learning rate. Thus, the connective weight w_l^6 is updated in accordance with the (24)

$$w_l^6(N+1) = w_l^6(N) + \Delta w_l^6. \tag{25}$$

2) Layer 5: The propagated two error terms in this layer are given by

$$\delta_l^5 = -\frac{\partial E}{\partial y_l^5(N)} = -\frac{\partial E}{\partial y_o^6(N)}\frac{\partial y_o^6(N)}{\partial y_l^5} = \delta_o^6 w_l^6 \tag{26}$$

$$\delta_{pl}^5 = -\frac{\partial E}{\partial y_{pl}^5(N)} = -\frac{\partial E}{\partial y_o^6(N)}\frac{\partial y_o^6(N)}{\partial y_l^5(N)}\frac{\partial y_l^5(N)}{\partial y_{pl}^5(N)} = \delta_l^5 \psi_k w_r^5 y_l^5(N-1). \tag{27}$$

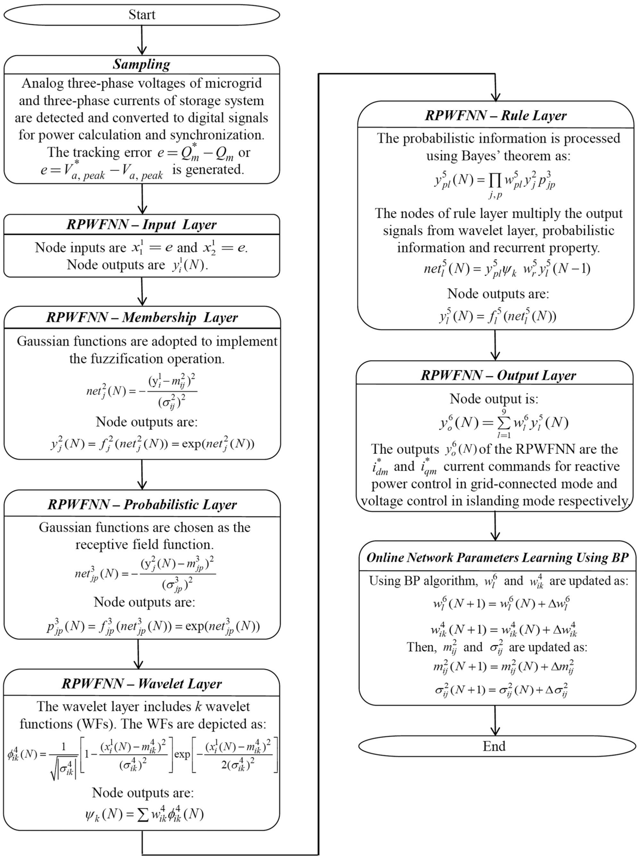

Fig. 4. Flowchart of proposed RPWFNN controller for active power control in grid-connected mode and voltage control in islanding mode.

3) Layer 4: The error term needs to be propagated in layer 4 is represented in the following:

$$\delta_{ik}^4 = -\frac{\partial E}{\partial \psi_k} = -\frac{\partial E}{\partial y_o^6(N)} \frac{\partial y_o^6(N)}{\partial y_l^5(N)} \frac{\partial y_l^5(N)}{\partial \psi_k(N)} = \delta_l^5 y_{pl}^5 w_r^5 y_l^5(N-1). \tag{28}$$

In accordance with the chain rule, the update law of the connective weight in layer 4 is calculated as

$$\Delta w_{ik}^4 = -\eta_2 \frac{\partial E}{\partial w_{ik}^4} = -\eta_2 \frac{\partial E}{\partial y_o^6(N)} \frac{\partial y_o^6(N)}{\partial y_l^5(N)} \frac{\partial y_l^5(N)}{\partial \psi_k(N)} \frac{\partial \psi_k(N)}{\partial w_{ik}^4(N)} = \eta_2 \delta_{ik}^4 \phi_{ik}^4 \tag{29}$$

where η_2 is the learning rate. Furthermore, the updated connective weight w_{ik}^4 is obtained as

$$w_{ik}^4(N+1) = w_{ik}^4(N) + \Delta w_{ik}^4. \tag{30}$$

4) Layer 2: The term of the propagated error in layer 2 is computed as

$$\delta_j^2 = -\frac{\partial E}{\partial net_j^2} = -\frac{\partial E}{\partial y_o^6(N)} \frac{\partial y_o^6(N)}{\partial y_l^5(N)} \frac{\partial y_l^5(N)}{\partial y_{pl}^5(N)} \frac{\partial y_{pl}^5(N)}{\partial y_j^2(N)} \frac{\partial y_j^2(N)}{\partial net_j^2(N)} = \sum_p \delta_{pl}^5 y_{pl}^5. \tag{31}$$

The updated amounts of the mean and the standard deviation of the membership functions in layer 2 are gained respectively according to the chain rule in the following:

$$\Delta m_{ij}^2 = -\eta_3 \frac{\partial E}{\partial m_{ij}^2} = -\eta_3 \frac{\partial E}{\partial y_o^6(N)} \frac{\partial y_o^6(N)}{\partial y_l^5(N)} \frac{\partial y_l^5(N)}{\partial y_{pl}^5(N)} \frac{\partial y_{pl}^5(N)}{\partial y_p^3(N)} \frac{\partial y_p^3(N)}{\partial y_j^2(N)} \times \frac{\partial y_j^2(N)}{\partial \mathrm{net}_\mathrm{j}^2(\mathrm{N})} \frac{\partial \mathrm{net}_\mathrm{j}^2(\mathrm{N})}{\partial m_{ij}^2(N)} = \eta_3 \delta_j^2 \frac{2(y_i^1 - m_{ij}^2)}{(\sigma_{ij}^2)^2} \tag{32}$$

$$\Delta \sigma_{ij}^2 = -\eta_4 \frac{\partial E}{\partial \sigma_{ij}^2} = -\eta_4 \frac{\partial E}{\partial y_o^6(N)} \frac{\partial y_o^6(N)}{\partial y_l^5(N)} \frac{\partial y_l^5(N)}{\partial y_{pl}^5(N)} \frac{\partial y_{pl}^5(N)}{\partial y_p^3(N)} \frac{\partial y_p^3(N)}{\partial y_j^2(N)} \times \frac{\partial y_j^2(N)}{\partial \mathrm{net}_\mathrm{j}^2(\mathrm{N})} \frac{\partial \mathrm{net}_j^2(N)}{\partial \sigma_{ij}^2(N)} = \eta_4 \delta_j^2 \frac{2(y_i^1 - m_{ij}^2)^2}{(\sigma_{ij}^2)^3} \tag{33}$$

where η_3 and η_4 are the learning rates. Hence, the mean and the standard deviation of the membership functions in layer 2 are updated in accordance with the following equations:

$$m_{ij}^2(N+1) = m_{ij}^2(N) + \Delta m_{ij}^2 \tag{34}$$

$$\sigma_{ij}^2(N+1) = \sigma_{ij}^2(N) + \Delta \sigma_{ij}^2. \tag{35}$$

Owing to the uncertainties of the storage system, the accurate calculation of the Jacobian of the storage system, $\partial Q_m / \partial y_o^6(N)$, cannot be gained. Thus, in order to solve this problem, the delta adaptation law is adopted as follows for increasing the online learning speed of the network parameters:

$$\delta_o \cong e + \dot{e}. \tag{36}$$

C. Procedure of Reactive Power Control and Voltage Control

The flowchart of the proposed RPWFNN controller for the reactive power control in grid-connected mode and voltage control in islanding mode is provided in Fig. 4 and described as follows.

1) Sampling: The analog three-phase voltages V_a, V_b, V_c of the microgrid and the three-phase currents i_{oa}, i_{ob}, i_{oc} of the storage system are detected by the voltage and current sensor circuits and converted to digital signals via an analog-to-digital converter in the DSP for the power calculation and synchronization. Then, the tracking error $e = Q_m^* - Q_m$ or

$e = V^*_{a,\text{peak}} - V_{a,\text{peak}}$ is generated and sent to the proposed RPWFNN controller.

2) RPWFNN Input Layer: The input variables of the proposed RPWFNN are e and $\dot{e}$. In the input layer, the node outputs are $y^1_i(N)$ and sent to the membership layer.

3) RPWFNN Membership Layer: The Gaussian functions are adopted to implement the fuzzification operation and the outputs are $y^2_j(N)$. Then, the outputs $y^2_j(N)$ are sent to the probabilistic layer.

4) RPWFNN Probabilistic Layer: In this layer, the Gaussian functions are also chosen as the receptive field function. The outputs are $p^3_{jp}(N)$ and sent to the rule layer.

5) RPWFNN Wavelet Layer: The wavelet layer includes k WFs. The input variables of this layer are e and $\dot{e}$. The, the node outputs ψ_k are obtained by performing the summation and multiplying operations and sent to the rule layer.

6) RPWFNN Rule Layer: This layer contains the rule layer and the recurrent layer. Moreover, the nodes of the rule layer multiply the output signals from the wavelet layer, probabilistic information and recurrent property, and output the result of the product for dynamic mapping. The outputs are $y^5_l(N)$ and sent to the output layer.

7) RPWFNN Output Layer: The node performs the summation operation and the output is given as $y^6_o(N)$.

Moreover, the output $y^6_o(N)$ of the proposed RPWFNN is the current command i^*_{dm} of storage system operated in the grid-connected mode for the reactive power control and the current command i^*_{qm} of storage system operated in islanding mode for the voltage control, respectively.

8) Online Network Parameters Learning Using BP: The online parameters learning is achieved by online tuning of the connective weights w^6_l between the output layer and the rule layer, the connective weights w^4_{ik} in the wavelet layer, and the mean m^2_{ij} and standard deviations σ^2_{ij} of the membership functions in the membership layer using the BP algorithm.

IV. EXPERIMENTAL SETUP AND EXPERIMENTATION

The experimental setup of the developed microgrid with a 3-kW varying resistive three-phase load is shown in Fig. 5. The block diagrams of the storage system and the PV system are presented in Fig. 5(a) and (b), respectively. In this article, the LiFePo4 battery is adopted as the storage system implemented by a Texas Instruments (TI) DSP TMS320F28335 with 1 ms sampling time shown in Fig. 5(a). The peripheral circuits comprise the voltage feedback, current feedback, interlocking circuit, and the protection circuit. Moreover, the control algorithms, including the virtual inertia, PLL, active/reactive power control, voltage/frequency control, and the proposed RPWFNN controller, are implemented by the control platform using the TI DSP TMS320F28335. The inertia constant M and the damping factor D are obtained by trial and error to achieve the best transient and steady-state responses of the active power of the storage system. The resulted inertia constant M and the damping factor D are 0.05 $(\text{kg}\cdot\text{m}^2)\text{rad/s}$ and 20, respectively. The switching frequency of the storage system is set to be 16 kHz. Furthermore, the LiFePo4 battery consists of six battery packs in series. Each battery pack is composed of 24 battery cells with 12 cells in series as a unit and 2 units in parallel. The nominal voltage and the capacity of the battery storage, the battery pack and the battery cell are 237.6 V/30 Ah, 39.6 V/30 Ah, and 3.3 V/15 Ah; the recommended charging voltage, the cut-off discharge voltage and the balance voltage of the battery cell are 3.5 V, 2.5 V, and 3.5 V, respectively. In addition, the PV system is implemented by a personal computer (PC) via the MATLAB & Simulink real-time control package with 0.5 ms sampling time shown in Fig. 5(b). The PV panel is emulated by using Chroma 62150H-6005. The three-phase voltages V_a, V_b, V_c of the microgrid and the three-phase currents i_{ou}, i_{ov}, i_{ow} of the PV system are detected and sent to the PC via the A/D converter on the PCI-1716 interface card for the power calculation and synchronization. The switching frequency of the PV system

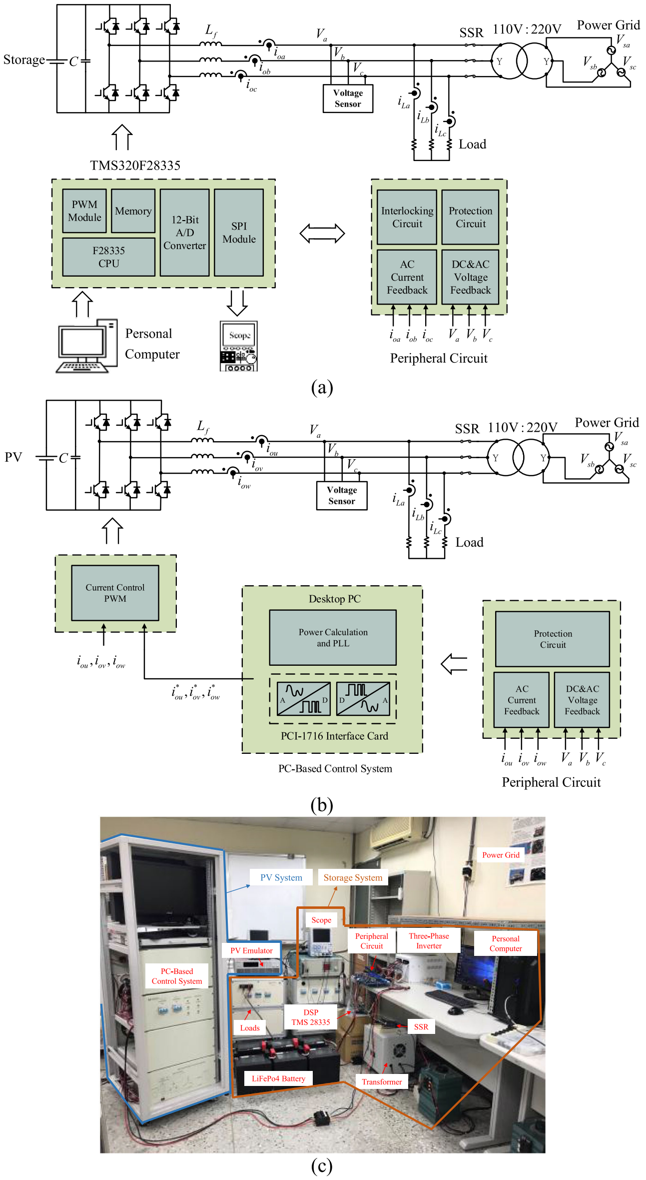

Fig. 5. Experimental setup of microgrid. (a) Block diagram of storage system. (b) Block diagram of PV system. (c) Photo of developed microgrid.

is set to be 10 kHz. Additionally, the open-circuit voltage and short circuit current of the emulated PV panel are 377.4 V and 5.632 A, respectively; the voltage, current and power output of the maximum power point (MPP) of the PV panel are 360 V, 5.556 A, and 2 kW. The photograph of the developed microgrid is provided in Fig. 5(c).

In order to verify the smart grid and the grid-forming capability of the developed microgrid with virtual inertia using the proposed RPWFNN controller, three test conditions, the grid-connected mode, switching between grid-connected mode and islanding mode, and islanding mode, are designed in the experimentation. Moreover, to compare the performance of the developed microgrid using the proposed RPWFNN controller, the experimental results using the PI controlled storage system of the microgrid are also provided for the demonstration.

A. Grid-Connected Mode

At this case, the microgrid with 1-kW load is operated in grid-connected mode. The active power command P_m^* of the storage system is changed from 0.5 to 1.5 kW and finally changed to 1 kW. The reactive power command Q_m^* of the storage system is changed from 0 Var to 0.5 kVar. Moreover, the active power command P_s^* and the reactive power command Q_s^* of the PV system are maintained to be 1.5 kW and 0 Var. The PV system is not operated at the MPP owing to the active power control. In the experimentation, first, in order to verify the effectiveness of the microgrid with virtual inertia using the master and slave control, the experimental result of the storage system using PI controllers without the virtual inertia is provided. The responses of the active power P_m and reactive power Q_m of the storage system using PI controllers without the virtual inertia are represented in Fig. 6(a). Moreover, the experimental results of the microgrid using PI controllers with the virtual inertia are provided in Fig. 6(b)–(d). The responses of the active power P_m and reactive power Q_m of the storage system using PI controllers with the virtual inertia are represented in Fig. 6(b). The responses of the active power P_s and reactive power Q_s of the PV system are shown in Fig. 6(c). The responses of the active power P_{grid} and reactive power Q_{grid} of the power grid are illustrated in Fig. 6(d). According to the experimental result shown in Fig. 6(a), the transient response of the active power P_m of the storage system using PI controller tracks the power command promptly due to the absence of the virtual inertia. On the other hand, the transient response of the active power P_m of the storage system using PI controllers with the virtual inertia tracks the power command smoothly, as shown in Fig. 6(b). Hence, the effectiveness and the feasibility of the microgrid with virtual inertia are verified. In general, a public grid exhibits the characteristics of a weak grid in which there is a grid impedance that cannot be ignored [35]. The weak grid will cause the oscillation of voltage and lead to the poor power quality and instability [35], [36]. The above-mentioned phenomena can be much improved by using the microgrid with virtual inertia. Furthermore, in accordance with the experimental results shown in Fig. 6(b)–(d), since the microgrid is equipped with 1-kW load, the extra active power and reactive power of the storage system and PV system are dispatched to the distributed power grid, as shown in Fig. 6(d). In addition, to improve the tracking control of the reactive power of the storage system, the RPWFNN controller is proposed to replace the traditional PI controller in the *d*-axis control current of the storage system shown in Fig. 2(a). Meanwhile, the *q*-axis control current of the storage system still adopts the PI controller with virtual inertia for the active power control. The experimental results of the microgrid using the proposed RPWFNN controller with the virtual inertia are shown in Fig. 6(e)–(g). The responses of the active power P_m using the PI controller and the reactive power Q_m using the proposed RPWFNN controller of the storage system with the virtual inertia are represented in Fig. 6(e). The responses of the active power P_s and reactive power Q_s of the PV system are illustrated in Fig. 6(f). The responses of the active power P_{grid} and reactive power Q_{grid} of the power grid are expressed in Fig. 6(g). Additionally, the response time of reactive power control of storage system using PI and the proposed RPWFNN controller operated in grid-connected mode is represented in Table I. According to the experimental results shown in Fig. 6(b) and (e) and Table I, the transient and steady-state responses of reactive power control of the RPWFNN controlled storage system are better than the PI controlled storage system due to the merits of the proposed RPWFNN controller such as the superior modeling performance and the capability to approximate the nonlinear systems and uncertainties. Moreover, the energy balance in the power flow of the microgrid in which the storage system uses the proposed RPWFNN controller is also verified, as shown in Fig. 6(e)–(g). Therefore, in this case, the effectiveness of the microgrid with virtual inertia using the master and slave control are validated. Consequently, the superior response of the reactive power control of the storage system using the proposed RPWFNN controller is also certified.

B. Switching Between Grid-Connected Mode and Islanding Mode

In this test case, the operation of the microgrid with 2-kW load is changed from the grid-connected mode in the interval 0–10 s to islanding mode in the interval 10–20 s due to the power grid fail at 10 s. The storage system and the PV system both adopts the active/reactive power control in grid-connected mode. Meanwhile, the voltage and frequency of the microgrid are imposed by the power grid. When the power grid interrupts, the storage system switches from the active/reactive power control to the voltage/frequency control to maintain the voltage and frequency of the microgrid. Moreover, the PV system still adopts the active/reactive power control in islanding mode. The active power command P_m^* and the reactive power command Q_m^* of the storage system are set to be 0.5 kW and 0 Var in grid-connected mode and the peak of the phase voltage command $V_{a,\text{peak}}^*$ and the frequency command f^* of the storage system are set to be 89 V and 60 Hz in islanding mode. The active power command P_s^* and the reactive power command Q_s^* of the PV system are maintained to be 0.5 kW and 0 Var in both the grid-connected mode and the islanding mode. First, the experimental results of the micrgorid using the conventional PI controller during the switching between the grid-connected mode and the islanding

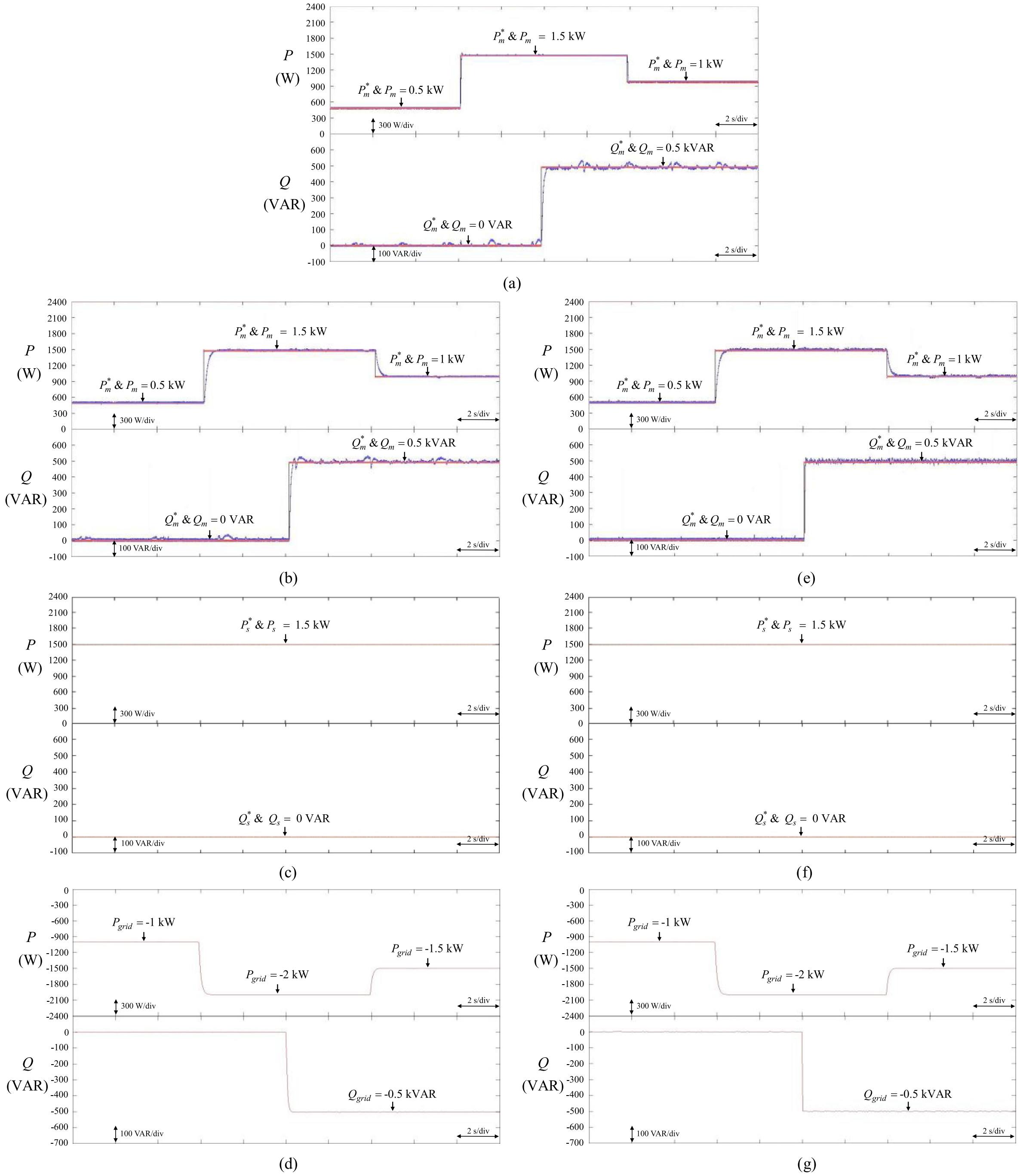

Fig. 6. Experimental results of microgrid operated in grid-connected mode. (a) Responses of active power and reactive power of storage system using PI controller without virtual inertia. (b) Responses of active power and reactive power of storage system using PI controller with virtual inertia. (c) Responses of active power and reactive power of PV system. (d) Responses of active power and reactive power of power grid. (e) Responses of active power and reactive power of storage system using proposed RPWFNN controller with virtual inertia. (f) Responses of active power and reactive power of PV system. (g) Responses of active power and reactive power of power grid.

TABLE I
RESPONSE TIME OF REACTIVE POWER CONTROL OF STORAGE SYSTEM USING PI AND RPWFNN OPERATED IN GRID-CONNECTED MODE

Case Condition	Reactive Power Controller	Response Time (s) Q_m : 0 VAR ⟶ 0.5 kVAR
Grid-Connected Mode	PI	0.4
	RPWFNN	0.12

mode are represented in Fig. 7(a)–(d). The responses of the peak of the *a*-phase voltage and the frequency of the microgrid using the conventional PI controller are shown in Fig. 7(a). The responses of active power and reactive power of the storage and the PV systems are represented in Fig. 7(b) and (c). The responses of active power and reactive power of the power grid are illustrated in Fig. 7(d). According to the experimental result shown in Fig. 7(a), though the steady-state response of

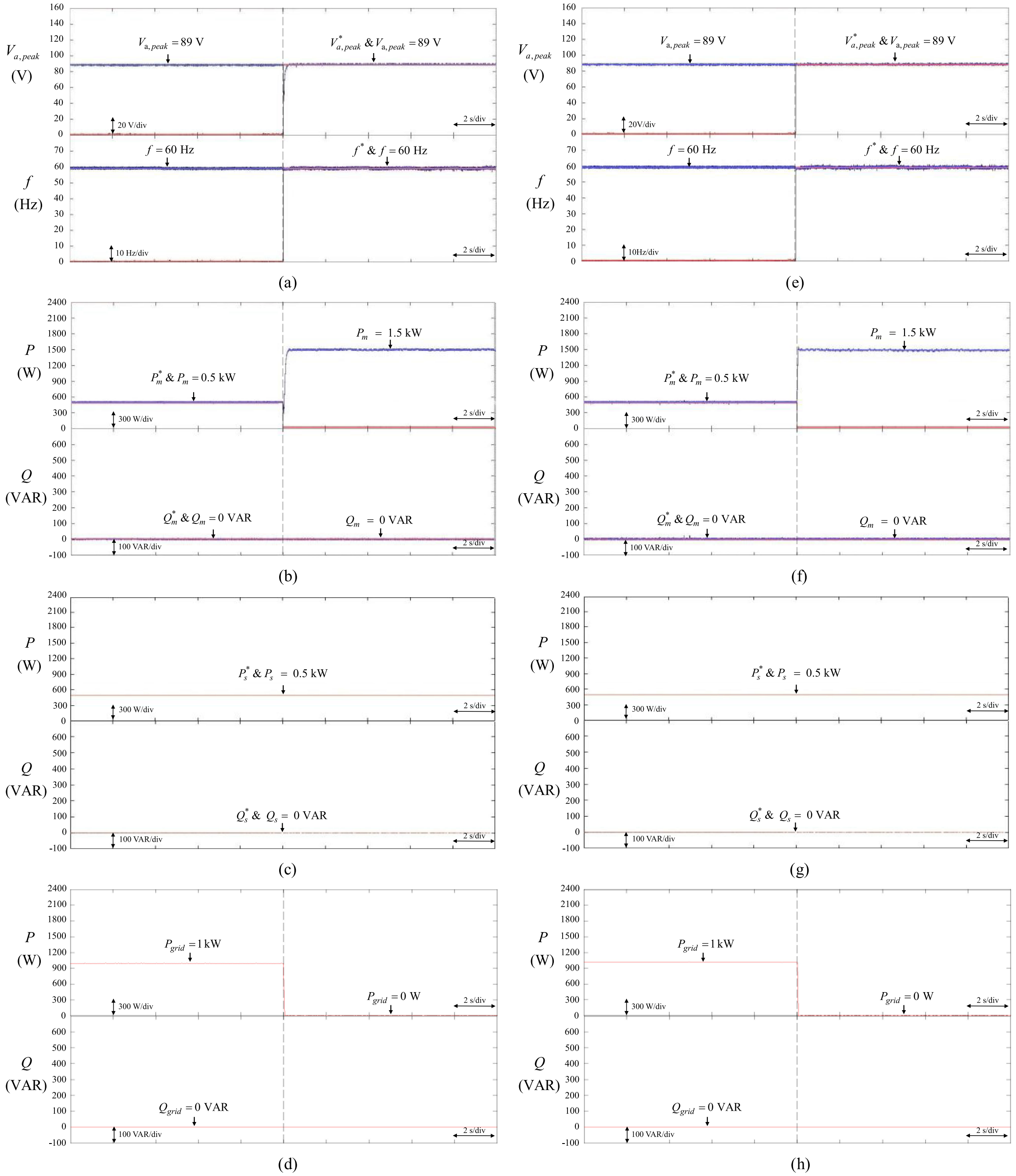

(a) (e)

(b) (f)

(c) (g)

(d) (h)

Fig. 7. Experimental results of microgrid during mode switching. (a) Responses of peak of a-phase voltage and frequency of microgrid using PI controller. (b) Responses of active power and reactive power of storage system. (c) Responses of active power and reactive power of PV system. (d) Responses of active power and reactive power of power grid. (e) Responses of peak of a-phase voltage and frequency of microgrid using proposed RPWFNN controller. (f) Responses of active power and reactive power of storage system. (g) Responses of active power and reactive power of PV system. (h) Responses of active power and reactive power of power grid.

the voltage of the microgrid can be maintained corresponding to the voltage command of the storage system in islanding mode, the transient response of the voltage of the microgrid fluctuates seriously during the mode switching due to the poor robustness of the PI controller. Furthermore, in the interval 0–10 s, since the microgrid with 2-kW load is connected with the power grid, the power grid delivers the active power 1 kW to the 2-kW load for the power demand shown in Fig. 7(b)–(d). When the microgrid operates in islanding mode in the interval 10–20 s, the delivered power from the power grid reduces to be zero. In addition, since the storage system adopts the voltage/frequency control in the islanding mode for maintaining the voltage and frequency, the storage system dispatches active power 1.5 kW to the load in accordance with the load demand. Thus, the power balance of supply and demand can be guaranteed.

In this article, to improve the transient response of the microgrid during the mode switching, the RPWFNN controller is also proposed to replace the traditional PI controller in q-axis

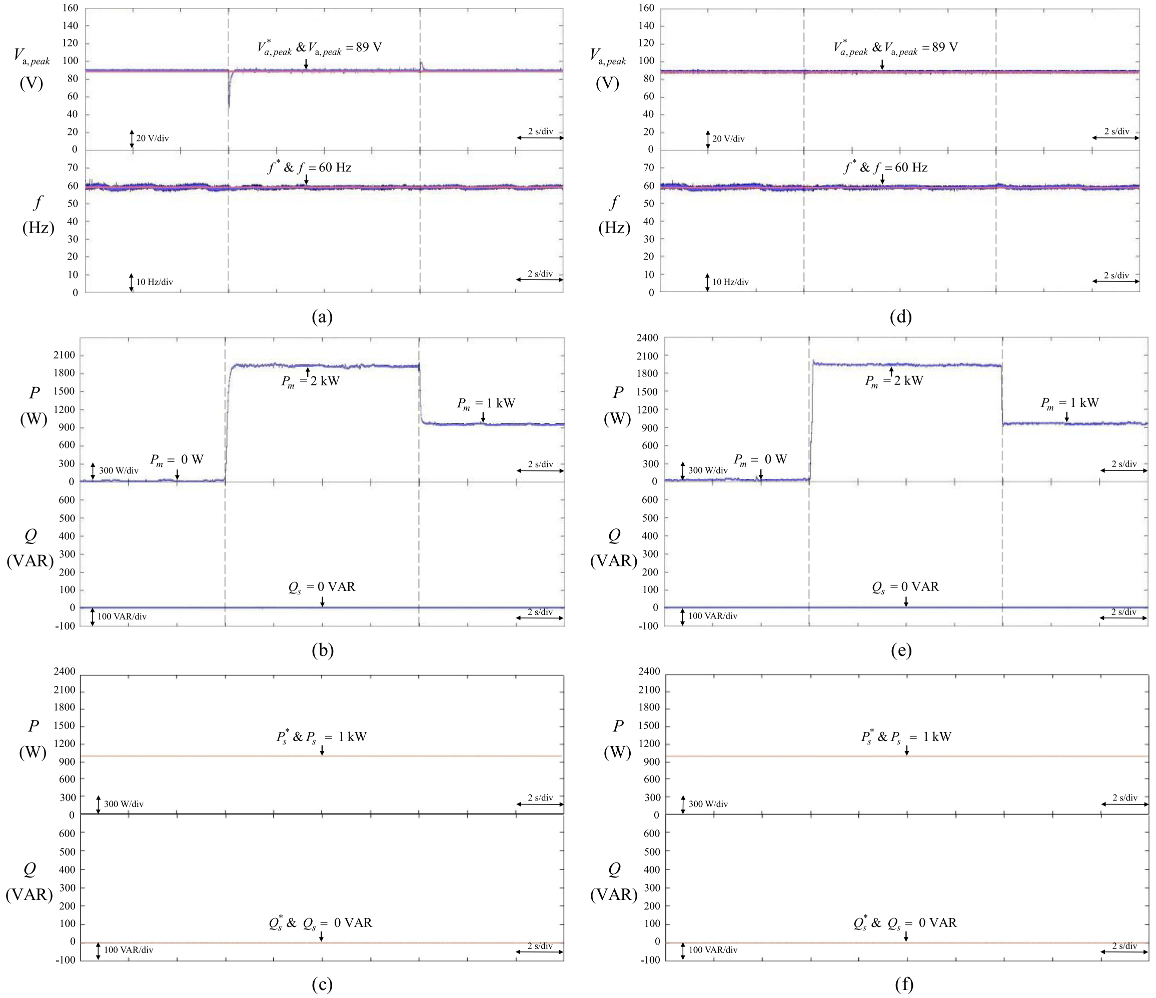

Fig. 8. Experimental results of microgrid operated in islanding mode under load variation. (a) Responses of peak of *a*-phase voltage and frequency of microgrid using PI controller. (b) Responses of active power and reactive power of storage system. (c) Responses of active power and reactive power of PV system. (d) Responses of peak of *a*-phase voltage and frequency of microgrid using proposed RPWFNN controller. (e) Responses of active power and reactive power of storage system. (f) Responses of active power and reactive power of PV system.

control current of the storage system operated in islanding mode for the voltage control, as shown in Fig. 2(b). The experimental results of the micrgorid using the proposed RPWFNN controller during the switching between the grid-connected mode and the islanding mode are represented in Fig. 7(e)–(h). The responses of the peak of the *a*-phase voltage and the frequency of the microgrid using the proposed RPWFNN controller are shown in Fig. 7(e). The responses of active power and reactive power of the storage and the PV systems are presented in Fig. 7(f) and (g). The responses of active power and reactive power of the power grid are provided in Fig. 7(h). Moreover, the response time and maximum voltage error of voltage control of microgrid using PI and the proposed RPWFNN controller during mode switching are shown in Table II. Comparing with the experimental result shown in Fig. 7(a) and Table II, the transient response of the voltage of the microgrid using the proposed RPWFNN controller shown in Fig. 7(e) owns better control performance during the mode switching owing to the robustness and the adaptivity of the proposed RPWFNN controller. Hence, the seamless switching of the microgrid can be achieved. Furthermore, the power balance of supply and demand can be guaranteed shown in Fig. 7(f)–(h).

TABLE II
RESPONSE TIME AND MAXIMUM VOLTAGE ERROR OF VOLTAGE CONTROL OF MICROGRID USING PI AND RPWFNN DURING MODE SWITCHING

Case Condition	Voltage Controller	Response Time (s)	Maximum Voltage Error (V)
Mode Switching	PI	0.289	42.6
	RPWFNN	0.031	1.2

C. Islanding Mode

In islanding mode, the voltage and frequency of the microgrid are controlled by the storage system. The active power command P_s^* and reactive power command Q_s^* of the PV system are maintained to be 1 kW and 0 Var, respectively. Moreover, to test the active/reactive power control performance of the microgrid

TABLE III
RESPONSE TIME AND MAXIMUM VOLTAGE ERROR OF VOLTAGE CONTROL OF MICROGRID USING PI AND RPWFNN OPERATED IN ISLANDING MODE UNDER LOAD VARIATION

Case Condition	Voltage Controller	Response Time (s)	Maximum Voltage Error (V)	Response Time (s)	Maximum Voltage Error (V)
		Load: 1 kW → 3 kW	Load: 1 kW → 3 kW	Load: 3 kW → 2 kW	Load: 3 kW → 2 kW
Islanding Mode	PI	0.321	43.4	0.271	9.4
	RPWFNN	0.035	8.2	0.028	3.9

under load variation, the load of the microgrid is changed from 1 to 3 kW and finally changed to 2 kW. First, the experimental results of the microgrid using the PI controller under load variation are provided in Fig. 8(a)–(c). The responses of the peak of the *a*-phase voltage and the frequency of the microgrid using the PI controller are shown in Fig. 8(a). The responses of active power and reactive power of the storage and the PV systems are presented in Fig. 8(b) and (c). In accordance with the experimental result shown in Fig. 8(a), the voltage of the microgrid controlled by the storage system using the PI controller fluctuates seriously at the moment of the load change. Moreover, the storage system delivers varying active powers to the load to match the power demand, as shown in Fig. 8(b). On the other hand, to improve the transient and steady-state responses of the voltage control of the microgrid under load variation, the PI controller is replaced by the proposed RPWFNN controller in the storage system. The experimental results of the microgrid using the proposed RPWFNN controller under load variation are illustrated in Fig. 8(d)–(f). The responses of the peak of the *a*-phase voltage and the frequency of the microgrid using the proposed RPWFNN controller are shown in Fig. 8(d). The responses of active power and reactive power of the storage and the PV systems are presented in Fig. 8(e) and (f). Furthermore, the response time and maximum voltage error of voltage control of microgrid using PI and the proposed RPWFNN controller operated in islanding mode under load variation are provided in Table III. According to the experimental results shown in Fig. 8(d) and Table III, since the proposed RPWFNN possesses the online learning ability and the ability of dealing with the time-varying inputs or outputs, the transient and steady-state responses of the voltage of the microgrid using the proposed RPWFNN controller under load variation can be effectively improved comparing with the PI controlled microgrid as shown in Fig. 8(a). Furthermore, the power balance of supply and demand can be guaranteed, as shown in Fig. 8(e) and (f). Therefore, the grid-forming capability of the microgrid using the proposed RPWFNN controller can be achieved.

In this article, the execution or compute time of the "C" program in the TMS320F28335 32-bit floating-point DSP with 150 MHz can be obtained by the clock tool of Texas Instruments (TI) Code Composer Studio (CCS) v6 program editing interface. The total operation cycles and total execution time of the storage system using PI and the proposed RPWFNN controller are compared in Table IV. The total operation cycles and total execution time for the proposed RPWFNN are 10856 cycles and 0.723 μs, respectively. As a result, the total execution time of the proposed RPWFNN is still less than 1 ms, which is the sampling interval of the control loop.

TABLE IV
EXECUTION TIME USING PI AND PROPOSED RPWFNN CONTROLLERS

Controllers	PI	Proposed RPWFNN
Total Operation Cycles	15	10856
Execution Time	0.1 μs	0.723 μs

V. CONCLUSION

In this article, a microgrid with virtual inertia using master–slave control has been successfully developed and implemented. The storage system and PV system are considered as the master unit and the slave unit, respectively, in the microgrid. Moreover, in order to improve the reactive power control performance in grid-connected mode and the transient response of the microgrid during the mode switching, an online trained RPWFNN is proposed and to replace the conventional PI controller in the storage system of the microgrid. Furthermore, since the load variation has serious influence on the voltage control of the microgrid operated in islanding mode, the proposed RPWFNN controller is also adopted to improve the transient and steady-state responses of the voltage of the microgrid under load variation. In addition, the effectiveness and the feasibility of the microgrid with virtual inertia using the proposed RPWFNN controller are certified by the experimental results. According to the experimental results, the seamless switching and the grid-forming capability of the microgrid using the proposed RPWFNN controller can be verified owing to the robustness and online training capability of the RPWFNN controller.

The major contributions of this article are as follows:

1) the successful development of a microgrid with virtual inertia using master–slave control;
2) the successful development of the proposed online trained RPWFNN controller;
3) the successful implementation of the microgrid using the proposed RPWFNN controller for the improvements of reactive power control, mode switching, and voltage control.

REFERENCES

[1] J. Liu, Y. Miura, and T. Ise, "Comparison of dynamic characteristics between virtual synchronous generator and droop control in inverter-based distributed generators," *IEEE Trans. Power Electron.*, vol. 31, no. 5, pp. 3600–3611, May 2016.

[2] G. C. Kryonidis, E. O. Kontis, A. I. Chrysochos, K. O. Oureilidis, C. S. Demoulias, and G. K. Papagiannis, "Power flow of islanded AC microgrids: Revisited," *IEEE Trans. Smart Grid*, vol 9, no. 4, pp. 3903–3905, Jul. 2018.

[3] A. Gupta, S. Doolla, and K. Chatterjee, "Hybrid AC-DC microgrid systematic evaluation of control strategies," *IEEE Trans. Smart Grid*, vol. 9, no. 4, pp. 3830–3843, Jul. 2018.

[4] K. H. Tan, F. J. Lin, J. H. Chen, and Y. R. Chang, "Intelligent controlled shunt active power filter for voltage and current harmonic compensation in microgrid system," *J. Chin. Inst. Eng.*, vol. 41, no. 4, pp. 269–285, Jun. 2018.

[5] C. S. Wang *et al.*, "A highly integrated and reconfigurable microgrid testbed with hybrid distributed energy sources," *IEEE Trans. Smart Grid*, vol. 7, no. 1, pp. 451–459, Jn. 2016.

[6] J. H. Jeon *et al.*, "Development of hardware in-the-loop simulation system for testing operation and control functions of microgrid," *IEEE Trans. Power Electron.*, vol. 25, no. 12, pp. 2919–2929, Dec. 2010.
[7] E. Hossain, E. Kabalci, R. Bayindir, and R. Perez, "A comprehensive study on microgrid technology," *Int. J. Renew. Energy Res.*, vol. 4, no. 4, pp. 1094–1107, 2014.
[8] D. E. Olivares *et al.*, "Trends in microgrid control," *IEEE Trans. Smart Grid*, vol. 5, no. 4, pp. 1905–1919, Jul. 2014.
[9] L. Meng *et al.*, "Review on control of DC microgrids and multiple microgrid clusters," *IEEE J. Emerg. Sel. Top. Power Electron.*, vol. 5, no. 3, pp. 928–948, Sep. 2017.
[10] Y. Han, K. Zhang, H. Li, E. A. A. Coelho, and J. M. Guerrero, "MAS-based distributed coordinated control and optimization in microgrid and microgrid clusters: a comprehensive overview," *IEEE Trans. Power Electron.*, vol. 33, no. 8, pp. 6488–6508, Aug. 2018.
[11] J. Liu, Y. Miura, H. Bevrani, and T. Ise, "Enhanced virtual synchronous generator control for parallel inverters in microgrids," *IEEE Trans. Smart Grid*, vol. 8, no. 5, pp. 2268–2277, Sep. 2017.
[12] K. Yu, Q. Ai, S. Wang, J. Ni, and T. Lv, "Analysis and optimization of droop controller for microgrid system based on small-signal dynamic model," *IEEE Trans. Smart Grid*, vol. 7, no. 2, pp. 695–705, Mar. 2016.
[13] J. Alipoor, Y. Miura, and T. Ise, "Power system stabilization using virtual synchronous generator with alternating moment of inertia," *IEEE J. Emerg. Sel. Top. Power Electron.*, vol. 3, no. 2, pp. 451–458, Jun. 2015.
[14] M. F. M. Arani and E. F. El-Saadany, "Implementing virtual inertia in DFIG-based wind power generation," *IEEE Trans. Power Syst.*, vol. 28, no. 2, pp. 1373–1384, May 2013.
[15] L. Y. Lu and C. C. Chu, "Consensus-based secondary frequency and voltage droop control of virtual synchronous generators for isolated AC micro-grids," *IEEE J. Emerg. Sel. Top. Circuits Syst.*, vol. 5, no. 3, pp. 443–455, Sep. 2015.
[16] S. Wang, J. Hu, X. Yuan, and L. Sun, "On inertial dynamics of virtual-synchronous-controlled DFIG-based wind turbines," *IEEE Trans. Energy Convers.*, vol. 30, no. 4, pp. 1691–1702, Dec. 2015.
[17] Y. Ma, W. Cao, L. Yang, F. Wang, and L. M. Tolbert, "Virtual synchronous generator control of full converter wind turbines with short-term energy storage," *IEEE Trans. Ind. Electron.*, vol. 64, no. 11, pp. 8821–8831, Nov. 2017.
[18] Q. C. Zhong, G. C. Konstantopoulos, B. Ren, and M. Krstic, "Improved synchronverters with bounded frequency and voltage for smart grid integration," *IEEE Trans. Smart Grid*, vol. 9, no. 2, pp. 786–796, Mar. 2018.
[19] T. Kerdphol, F. S. Rahman, Y. Mitani, M. Watanabe, and S. Küfeoğlu, "Robust virtual inertia control of an islanded microgrid considering high penetration of renewable energy," *IEEE Access*, vol. 6, pp. 625–636, Feb. 2018.
[20] H. Zhao, Q. Yang, and H. Zeng, "Multi-loop virtual synchronous generator control of inverter-based DGs under microgrid dynamics," *IET Gener. Transm. Distrib.*, vol. 11, no. 3, pp. 795–803, Feb. 2017.
[21] F. J. Lin, K. H. Tan, and D. Y. Fang, "Squirrel-cage induction generator system using hybrid wavelet fuzzy neural network control for wind power applications," *Neural Comput. Appl.*, vol. 26, no. 4, pp. 911–928, May 2015.
[22] F. J. Lin, Y. S. Huang, K. H. Tan, J. H. Chiu, and Y. R. Chang, "Active islanding detection method using D-axis disturbance signal injection with intelligent control," *IET Gener. Transm. Distrib.*, vol. 7, no. 5, pp. 537–550, May 2013.
[23] Y. Jin, C. Shan, Y. Wu, Y. Xia, Y. Zhang, and L. Zeng, "Fault diagnosis of hydraulic seal wear and internal leakage using wavelets and wavelet neural network," *IEEE Trans. Instrum. Meas.*, vol. 68, no. 4, pp. 1026–1034, Apr. 2019.
[24] J. C. Yin, A. N. Perakis, and N. Wang, "An ensemble real-time tidal level prediction mechanism using multiresolution wavelet decomposition method," *IEEE Trans. Geosci. Remote Sensing*, vol. 56, no. 8, pp. 4856–4865, Aug. 2018.
[25] P. A. Kowalski and M. Kusy, "Sensitivity analysis for probabilistic neural network structure reduction," *IEEE Trans. Neural Netw. Learn. Syst.*, vol. 29, no. 5, pp. 1919–1932, May 2018.
[26] M. Kusy and R. Zajdel, "Application of reinforcement learning algorithms for the adaptive computation of the smoothing parameter for probabilistic neural network," *IEEE Trans. Neural Netw. Learn. Syst.*, vol. 26, no. 9, pp. 2163–2175, Sep. 2015.
[27] K. H. Tan, F. J. Lin, and J. H. Chen, "DC-link voltage regulation using RPFNN-AMF for three-phase active power filter," *IEEE Access*, vol. 6, pp. 37454–37463, Jun. 2018.
[28] M. Xiao, W. X. Zheng, G. Jiang, and J. Cao, "Undamped oscillations generated by hopf bifurcations in fractional-order recurrent neural networks with caputo derivative," *IEEE Trans. Neural Netw. Learn. Syst.*, vol. 26, no. 12, pp. 3201–3214, Dec. 2015.
[29] Z. Zuo *et al.*, "Learning contextual dependence with convolutional hierarchical recurrent neural networks," *IEEE Trans. Image Process.*, vol. 25, no. 7, pp. 2983–2996, Jul. 2016.
[30] M. Lopez-Martin, B. Carro, A. Sanchez-Esguevillas, and J. Lloret, "Network traffic classifier with convolutional and recurrent neural networks for internet of things," *IEEE Access*, vol. 5, 18042–18050, Sep. 2017.
[31] Z. H. Ling, Y. Ai, Y. Gu, and L. R. Dai, "Waveform modeling and generation using hierarchical recurrent neural networks for speech bandwidth extension," *IEEE/ACM Trans. Audio Speech Lang. Process.*, vol. 26, no. 5, pp. 883–894, May 2018.
[32] F. J. Lin, K. C. Lu, and B. H. Yang, "Recurrent fuzzy cerebellar model articulation neural network based power control of single-stage three-phase grid-connected photovoltaic system during grid faults," *IEEE Trans. Ind. Electron.*, vol. 64, no. 2, pp. 1258–1268, Feb. 2017.
[33] S. Teimourzadeh, F. Aminifar, M. Davarpanah, and M. Shahidehpour, "Adaptive control of microgrid security," *IEEE Trans. Smart Grid*, vol. 9, no. 4, pp. 3909–3910, Jul. 2018.
[34] J. Fang, H. Li, Y. Tang, and F. Blaabjerg, "Distributed power system virtual inertia implemented by grid-connected power converters," *IEEE Trans. Power Electronic.*, vol. 33, no. 10, pp. 8488–8499, Oct. 2018.
[35] L. J. Cai and I. Erlich, "Doubly fed induction generator controller design for the stable operation in weak grids," *IEEE Trans. Sustain. Energy*, vol. 6, no. 3, pp. 1078–1084, Jul. 2015.
[36] D. Wu, G. Li, M. Javadi, A. M. Malyscheff, M. Hong, and J. N. Jiang, "Assessing impact of renewable energy integration on system strength using site-dependent short circuit ratio," *IEEE Trans. Sustain. Energy*, vol. 9, no. 3, pp. 1072–1080, Jul. 2018.

Kuang-Hsiung Tan received the B.S., M.S., and Ph.D. degrees from the Chung Cheng Institute of Technology (CCIT), National Defense University, Taiwan, ROC in 2002, 2007, and 2013, respectively, all in electrical and electronic engineering.

He has been a Faculty Member at CCIT, where he is currently an Associate Professor with the Department of Electrical and Electronic Engineering. His teaching and research interests include power electronics, power quality, microgrid systems, and intelligent control.

Faa-Jeng Lin (M'93–SM'99–F'17) received the B.S. and M.S. degrees in electrical engineering from National Cheng Kung University, Taiwan, in 1983 and 1985, respectively, and the Ph.D. degree in electrical engineering from National Tsing Hua University, Taiwan, in 1993.

He is currently a Chair Professor with the Department of Electrical Engineering, National Central University, Taiwan. His work has been widely cited. Several of his papers have helped to establish research areas such as fuzzy neural network control of motor drives and motion control systems, and resonant converters for piezo-ceramic motor drives. His research interests include ac motor drives, power electronics, renewable energies, smart grids, and intelligent and nonlinear control theories.

Dr. Lin was an Associate Editor of IEEE TRANSACTIONS ON FUZZY SYSTEMS. He also was the President with Taiwan Smart Grid Industry Association, from 2012 to 2016, and the Chair and Principle Investigator of Smart Grid Focus Center, National Energy Project Phase I and II in Taiwan, from 2011 to 2019. He is currently an Associate Editor of IEEE TRANSACTIONS ON POWER ELECTRONICS and the Executive Director of Taiwan Power Company. He is also an IET Fellow. He was the recipient of the Outstanding Research Awards from the National Science Council, Taiwan, in 2004, 2010, and 2013, and the Outstanding Professor of Engineering Award in 2016 from the Chinese Institute of Engineers, Taiwan.

Cheng-Ming Shih received the B.S. degree in electrical engineering from the Oriental Institute of Technology, New Taipei, Taiwan, in 2017, and the M.S. degree in electrical engineering from National Central University, Chungli, Taiwan, in 2019.

His research interests include microgrid systems, storage systems, virtual inertia, and intelligent control.

Che-Nan Kuo received the B.S. degree in electrical engineering from the National Changhua University of Education, Changhua, Taiwan, in 2018. He is currently working toward the M.S. degree with National Central University, Chungli, Taiwan.

His research interests include virtual synchronous generators, intelligent control, and PV systems.